

# Black holes surrounded by generic dark matter profiles: appearance and gravitational-wave emission

Enzo Figueiredo,<sup>1,2</sup> Andrea Maselli,<sup>2,3</sup> and Vitor Cardoso<sup>4,5</sup>

<sup>1</sup>*Département de Physique, ENS de Lyon, Univ. Claude Bernard, F-69342 Lyon, France*

<sup>2</sup>*Gran Sasso Science Institute (GSSI), I-67100 L'Aquila, Italy*

<sup>3</sup>*INFN, Laboratori Nazionali del Gran Sasso, I-67100 Assergi, Italy*

<sup>4</sup>*Niels Bohr International Academy, Niels Bohr Institute, Blegdamsvej 17, 2100 Copenhagen, Denmark*

<sup>5</sup>*CENTRA, Departamento de Física, Instituto Superior Técnico – IST,*

*Universidade de Lisboa – UL, Avenida Rovisco Pais 1, 1049 Lisboa, Portugal*

We develop a numerical approach to find asymptotically flat black hole solutions coupled to anisotropic fluids, described by generic density profiles. Our model allows for a variety of applications in realistic astrophysical scenarios, and is potentially able to describe the geometry of galaxies hosting supermassive black holes, dark matter environments and accretion phenomena. We apply our framework to a black hole surrounded by different families of dark matter profiles, namely the Hernquist, the Navarro-Frenk White and the Einasto models. We study the geodesic motion of light and of massive particles in such spacetimes. Moreover we compute gravitational axial perturbations induced by a small secondary on the numerical background, and determine the changes in the emitted gravitational wave fluxes compared to the vacuum case. Our analysis confirms and extend previous studies showing that modifications of orbital frequencies and axial fluxes can be described in terms of gravitational-redshift, regardless of the halo model.

## I. INTRODUCTION

Astrophysical compact sources do not live in vacuum, but rather evolve embedded in a complex environment of plasma, electromagnetic fields, and dark matter (DM), which is expected to leave detectable imprints on the dynamics and emitted gravitational wave (GW) signals of these systems [1–7].

Modifications to the orbital phase due to environmental effects provide a new route to determine the properties of the astrophysical arena where binaries evolve. Exploiting such effects can allow to probe a variety of fundamental astro-physics models including the formation channels of compact binaries [8, 9], the distribution of baryonic and dark matter surrounding massive objects [10–16], as well as the existence of new fundamental fields coupled to the gravity sector [17, 18]. Understanding how matter distribution affects the dynamics of coalescing binaries, and characterise the imprint left on the GW generation and propagation mechanisms, requires fully relativistic solutions that describe black holes (BHs) within a medium.

So far, however, most studies have mainly worked on Newtonian inspired corrections, or computed changes in the leading quadrupolar GW emission to assess the relevance of non-vacuum contributions [19, 20]. Few calculations that included relativistic corrections to the background spacetime or to dynamical friction highlighted the relevance of such terms, which also lead in general to larger modifications to the emitted signals [14, 21–23]. Moreover, all the investigations carried out so far to model GW signals, work within a post-Newtonian framework, which provides the best approach to describe nearly equal mass systems, but loses its validity for asymmetric binaries, and in particular for their more extreme configurations, which are expected to provide the tightest constraints on environmental parameters [3].

Such studies however highlight a key feature common to the vast majority of studies on environmental effects: corrections to the binary evolution tend to affect the low frequency inspiral regime, where coalescing binaries accumulate tens of hundreds of orbital cycles in the detector bandwidth of next generation of detectors. Developing precise models for BH solutions and the emitted GW signals is therefore even more pressing, given the accuracy requirements that such future observations will demand.

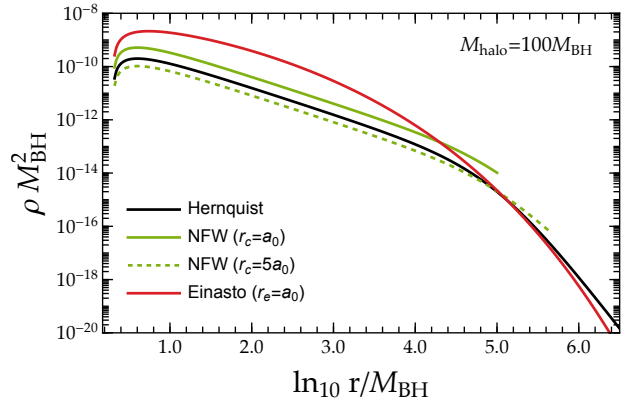


FIG. 1. Halo density profiles considered in this work as a function of the distance from the BH (in Schwarzschild-like coordinates), for a specific configuration with  $M_{\text{halo}} = 100M_{\text{BH}}$  and  $a_0 = 10^5 M_{\text{BH}}$ .

Recently, some of the present authors worked out the first spacetime geometry generated by a non-spinning BH within a core of matter [4]. This background was exploited to compute the GW fluxes emitted by extreme mass ratio inspirals (EMRIs), taking into account the coupling between fluid and gravitational perturbations in the full relativistic theory [24]. While these works

provide the first setup to study BH physics in realistic dense environments, they assumed a specific choice for the matter distribution, given by the Hernquist model [25], which allows to compute the metric in a closed analytical form.

In this paper we take a step further, and develop a new framework which extends the domain of applicability of the solution devised in Ref. [4] to generic matter profiles. We build a numerical pipeline to compute the spacetime geometry of spherically symmetric, and asymptotically flat BHs, within a spherically symmetric environment. The corresponding matter can be orders of magnitude larger than the BH itself, in which case our solution may describe, for example, a galactic DM halo. But the geometry could describe some more exotic physics, like a BH surrounded by a small-scale matter structure. We apply this formalism to investigate the effect of different families of DM halos on the BH geometry, and its geodesic structure. We also compute axial gravitational perturbations induced by a point-like on circular motion around the BH, and determine the changes onto the GW fluxes in terms of the halo properties. Hereafter we use geometric units  $G = c = 1$ .

## II. BACKGROUND AND AXIAL MODES

In this Section we summarize the key equations that describe a static, spherically symmetric BH spacetime embedded in an environment with a generic density profile  $\rho(r)$ . We refer the reader to [6, 24] for an extensive discussion, as well for technical details on the formalism, which has been originally applied to study binary BHs with an Hernquist-type matter distribution [25].

We adopt the Einstein cluster approach to model a stationary BH surrounded by a collection of gravitating masses [26]. In this framework the background metric specified by the line element

$$ds^2 = g_{\mu\nu}^{(0)} dx^\mu dx^\nu = -a(r)dt^2 + \frac{dr^2}{1 - \frac{2m(r)}{r}} + r^2 d\Omega^2, \quad (1)$$

is a solution of the sourced Einstein's field equations

$$G_{\mu\nu}^{(0)} = 8\pi T_{\mu\nu}^{(0)\text{env}}, \quad (2)$$

where the properties of the environment are encoded by the anisotropic stress-energy tensor with the following form:

$$(T^{(0)\text{env}})^\mu{}_\nu = \text{diag}(-\rho, 0, P_t, P_t). \quad (3)$$

For a given choice of  $\rho(r)$ , the mass profile is determined by the continuity equation  $m'(r) = 4\pi r^2 \rho(r)$ , while the metric variable  $a(r)$  and the tangential pressure are determined by the  $rr$  component of Eqs. (2) and by the Bianchi identities, respectively:

$$\frac{a'(r)}{a(r)} = \frac{2m(r)/r}{r - 2m(r)}, \quad P_t(r) = \frac{m(r)/2}{r - 2m(r)} \rho(r), \quad (4)$$

where a prime denotes a derivative with respect to the radial coordinate. Equations (4) completely specify the background solution. However, unlike the Hernquist profile which allows to compute metric and matter quantities in a closed analytical form, hereafter we focus on generic density distributions which requires a fully numerical treatment. As we shall describe in the next section, such numerical pipeline will only require as starting point a tabulated input for  $\rho(r)$ .

The solution for  $a(r)$  and  $m(r)$  also determines the geodesic properties for massive and massless particles. As for the vacuum Schwarzschild counterpart, the spacetime admits a timelike and a spacelike Killing vector associated with two conserved quantities, which can be identified with the energy per unit mass and the specific angular momentum at infinity:

$$E = \left[ \frac{r - 2m(r)}{r - 3m(r)} a(r) \right]_{r=r_p}^{1/2}, \quad L = \left[ \frac{m(r)}{r - 3m(r)} \right]_{r=r_p}^{1/2}. \quad (5)$$

where  $r_p$  identifies the particle orbital radius. Geodesics are planar and without loss of generality we assume  $\theta(r = r_p) = \pi/2$ . For massive objects the radius of the innermost circular orbit (ISCO)  $r_{\text{ISCO}}$  is given by a solution of the following equation

$$r^2 m'(r) + r m(r) - 6m^2(r) = 0, \quad (6)$$

with the corresponding angular frequency

$$\Omega_{\text{ISCO}} = \left[ \frac{1}{r^2} \frac{a(r)m(r)}{r - 2m(r)} \right]_{r=r_{\text{ISCO}}}^{1/2}. \quad (7)$$

Similarly, for massless particles the light-ring is determined by solving the equation  $r - 3m(r) = 0$ , and its frequency given by

$$\Omega_{\text{LR}} = \frac{\sqrt{a(r_{\text{LR}})}}{r_{\text{LR}}}. \quad (8)$$

With the background solution in hand we can study how GW propagation and generation change due to the environment. We focus on astrophysical scenarios provided by EMRIs, in which a secondary stellar mass object orbits the primary BH inducing perturbations of the metric and the stress-energy tensor

$$g_{\mu\nu} = g_{\mu\nu}^{(0)} + g_{\mu\nu}^{(1)}, \quad T_{\mu\nu}^{\text{env}} = T_{\mu\nu}^{(0)\text{env}} + T_{\mu\nu}^{(1)\text{env}}. \quad (9)$$

The first order terms  $g_{\mu\nu}^{(1)}$  and  $T_{\mu\nu}^{(1)\text{env}}$  are decomposed into standard axial and polar modes [27–30] and satisfy the perturbed field equations

$$G_{\mu\nu}^{(1)} = 8\pi T_{\mu\nu}^{(1)\text{env}} + 8\pi T_{\mu\nu}^p, \quad (10)$$

where  $T_{\mu\nu}^p$  is the stress-energy tensor associated to the secondary binary component with mass  $m_p$ . Hereafter we focus on axial type perturbations only, referring to the polar sector for a future study. In this case, metric

fluctuations decouple from matter variables and can be cast into a single Schrodinger-like equation for the master function  $\psi_{\ell m}(r)$ :

$$\frac{d^2 \psi_{\ell m}(r)}{dr_*^2} + [\omega^2 - V_\ell(r)] \psi_{\ell m}(r) = \mathcal{S}_{\ell m} , \quad (11)$$

where  $\ell = 2, \dots, \infty$ ,  $m = -\ell \dots \ell$ ,  $r^*$  is the tortoise coordinate defined as  $dr^*/dr = [a(r)(1 - 2m(r)/r)]^{-1/2}$  and the scattering potential reads

$$V_\ell(r) = \frac{a(r)}{r^2} \left[ \ell(\ell + 1) - \frac{6m(r)}{r} + m'(r) \right] . \quad (12)$$

For circular orbits the source term  $\mathcal{S}_{\ell m}$  can be written as:

$$\mathcal{S}_{\ell m} = 8i\pi \sqrt{2a(r)} \sqrt{1 - \frac{2m(r)}{r}} \Lambda_\ell r [a(r) \mathcal{D}_{\ell m}(r)]' , \quad (13)$$

with  $\Lambda_\ell = [\ell(\ell + 1)(\ell - 1)(\ell + 2)]^{-1/2}$  and

$$\mathcal{D}_{\ell m} = m \Lambda_\ell m_p \frac{L^2}{E} \sqrt{\frac{a(r)(r - 2m(r))}{2r^9}} \delta(r - r_p) \times \delta(\omega - m\omega_p) \frac{\partial}{\partial \theta} Y_{\ell m} \Big|_{\theta=\pi/2, \phi=0} , \quad (14)$$

where  $Y_{\ell m}(\theta, \phi)$  are the standard spherical harmonics, and  $\omega_p$  is the secondary orbital frequency evaluated at  $r = r_p$ . For  $m(r) = M_{\text{BH}}$  Eq. (11) reduces to the well-known Regge-Wheeler equation.

### The environmental density profiles

We consider parametric density distributions described by the following semi-analytic relation:

$$\rho(r) = \rho_0 (r/a_0)^{-\gamma} [1 + (r/a_0)^\alpha]^{(\gamma-\beta)/\alpha} . \quad (15)$$

For a given choice of the coefficients  $(\alpha, \beta, \gamma)$ , Eq. (15) identifies a family of profiles in which  $\beta$  and  $\gamma$  determine the dependence of the profile at large and small distances, respectively, with the sharpness of the transition given by  $\alpha$  [31]. The slope of the distribution changes at a characteristic spatial scale determined by  $a_0$ , with  $\rho_0$  being the corresponding density. Here we focus on two models, commonly used to interpret DM distribution emerging from numerical simulations and astrophysical observations: (i) the Hernquist profile corresponding to  $(\alpha, \beta, \gamma) = (1, 4, 1)$  [25] and, (ii) the Navarro-Frenk-White (NFW) distribution obtained by fixing  $(\alpha, \beta, \gamma) = (1, 3, 1)$  [32]. It is known that the NFW model predicts a mass function which diverges logarithmically with  $r$ . For this reason we prescribe a radial cut-off  $r_c$ , such that  $M_{\text{halo}}(r > r_c) = 0$ . We will analyse how this parameter affects the geodesic properties of the spacetime, and the emitted axial fluxes. Along with profiles inspired by Eq. (15), we also exploit our framework to study the  $1/r^n$  Einasto model [33]:

$$\rho(r) = \rho_e \exp \left\{ -d_n [(r/r_e)^{1/n} - 1] \right\} , \quad (16)$$

with  $n = 6$ ,  $d_n \sim 17.67$  [31, 34], and  $\rho_e$  being the density at the radius  $r_e$  that defines a volume containing half of the halo mass, fixed hereafter to  $r_e = a_0$ .

Newtonian and relativistic analyses show that density profiles with a BH sitting at their core, vanish at the horizon, and develop a cusp with a lengthscale dictated by the BH mass [23, 35]. The details of the overdensity depends on the specific form of the profile, and may be relevant for an accurate modelling of the GW signals emitted by coalescing binaries [14]. However, for the purpose of this work we encode the features of the accretion growth by re-scaling the density profile according to  $\rho(r) \rightarrow \rho(r)(1 - 2M_{\text{BH}}/r)$ , following the results of [4]. A full numerical treatment of the DM accretion onto the BH will be discussed in a forthcoming work, in which we will also extend current calculations to integrate polar perturbations for generic density profiles. Figure 1 shows the behavior of  $\rho(r)$  for the three cases described above, for prototype choices of  $(M_{\text{halo}}, a_0, r_c, r_e)$ .

### III. NUMERICAL PROCEDURE

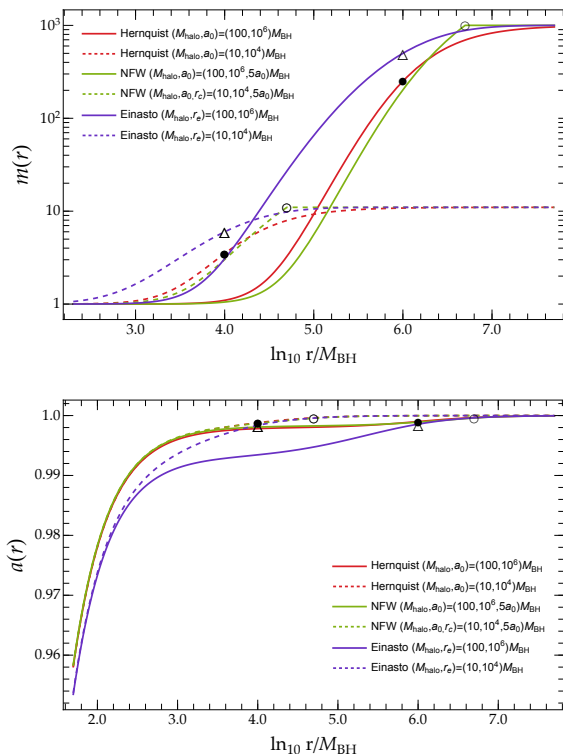


FIG. 2. Metric components  $m(r)$  and  $a(r)$  as a function of the coordinate radius, for different profiles and configurations. Black dots, empty circles and empty triangles along curves identify the value of  $a_0$ ,  $r_c$  and  $r_e$  for the Hernquist, NFW and Einasto model, respectively.

We have solved the background and the perturbation equations according to the following numerical procedure:

1. We start by choosing a density profile  $\rho(r)$  according to the Hernquist, the NFW or the Einasto model. We integrate the equation for the mass function  $m(r)$  from the horizon  $r_h = 2M_{\text{BH}}$ , where  $m(r_h) = M_{\text{BH}}$ , to a coordinate radius  $r_{\text{out}}$  that corresponds to our spatial infinity, and which guarantees asymptotic flatness. We take  $r_{\text{out}} \gtrsim 10^7 a_0$ . Changing this value by more than three orders of magnitude does not affect our results. We then solve backward the equation for the metric function  $a(r)$  assuming as initial condition in the far field limit that  $m(r \rightarrow r_{\text{out}}) = M_{\text{BH}} + M_{\text{halo}}$  and

$$a(r) = 1 - \frac{2(M_{\text{BH}} + M_{\text{halo}})}{r} + \mathcal{O}(1/r^3) . \quad (17)$$

Note that  $M_{\text{halo}}$  is therefore the total environmental mass outside the BH. As we explained, although geared towards DM distributions our results and techniques are applicable to any spherically symmetric environment. Examples of metric functions  $a(r)$  and  $m(r)$  are shown in Fig. 2.

2. The numerical solution for  $m(r)$  and  $a(r)$  allows to compute the tangential pressure  $P_t(r)$ , as well as the geodesic quantities, like the ISCO and the light ring frequencies,  $\Omega_{\text{ISCO}}$  and  $\Omega_{\text{LR}}$ .
3. We integrate the master equation (11) for  $\psi_{\ell m}$  using a standard Green function approach [24]. We first solve the associated homogeneous problem requiring that the physical solution satisfies pure incoming/outgoing wave boundary condition at the horizon and at infinity, namely:

$$\begin{aligned} \psi_{\ell m}^{(\text{in})} &= e^{-i\omega r_*} \sum_{i=0}^{n_{\text{in}}} \alpha_i (r - r_h)^i , \\ \psi_{\ell m}^{(\text{out})} &= e^{+i\omega r_*} \sum_{i=0}^{n_{\text{out}}} \frac{\beta_i}{r^i} , \end{aligned} \quad (18)$$

where we fix<sup>1</sup>  $n_{\text{in}} = n_{\text{out}} = 5$ . The coefficients  $(a_i, b_i)$  are obtained by solving the homogeneous equation at each order in  $(r - r_h)$  and  $1/r$ , and setting  $\alpha_0 = \beta_0 = 1$ . To this aim we also need to expand the metric functions  $m(r)$  and  $a(r)$  at both boundaries. At the horizon we consider the following ansatz:

$$m(r) = M_{\text{BH}} + \sum_{i=1}^{n_{\text{in}}} m^{(i)}(r_h)(r - r_h)^i , \quad (19)$$

$$a(r) = \sum_{i=1}^{n_{\text{in}}} a^{(i)}(r_h)(r - r_h)^i , \quad (20)$$

where the coefficients are found numerically using the interpolated numerical solutions for  $m(r)$  and  $a(r)$  found at step 1. At infinity we assume consistently that  $m(r_{\text{out}}) = M_{\text{BH}} + M_{\text{halo}}$  and  $a(r_{\text{out}}) = 1 - 2(M_{\text{BH}} + M_{\text{halo}})/r_{\text{out}}$ . The full solution at infinity is then obtained integrating the homogeneous component over the source term:

$$\begin{aligned} \psi_{\ell m}^{\text{out}} &= \lim_{r_* \rightarrow r_{\text{out}}} \psi_{\ell m}(r_*) \\ &= e^{+i\omega r_*} \int_{r_h}^{r_{\text{out}}} \frac{\psi_{\ell m}^{(r_h)} S_{\ell m}}{W} dr_* , \end{aligned} \quad (21)$$

where  $W = d\psi_{\ell m}^{(\text{out})}/dr_* \psi_{\ell m}^{(\text{in})} - d\psi_{\ell m}^{(\text{in})}/dr_* \psi_{\ell m}^{(\text{out})}$  is the Wronskian.

4. From Eq. (21) we obtain for each multipole component  $(\ell, m)$  the GW flux at infinity:

$$\dot{E}_{\ell m}^{\infty} = \frac{1}{16\pi} \frac{(\ell + 2)!}{(\ell - 2)!} |\psi_{\ell m}|^2 \quad (\ell + m \text{ odd}) . \quad (22)$$

The codes developed to integrate the background and the first order equations are freely available as a **Mathematica** package at [36].

## IV. RESULTS

### A. Geodesic properties

Our numerical approach allows us to study, along with the axial perturbations, the geodesic properties of the background.

The orbital frequencies at the light-ring and at the ISCO, are key to determine the observational signatures of bodies and radiation surrounding the BH [37, 38]. The frequency, as measured by far-away observers, is shown in the top row of Figure 3,  $\Omega_{\text{LR}}$ , normalized to the Schwarzschild value  $\Omega_{\text{LR}}^{\text{Scw}} = 1/(3\sqrt{3}M_{\text{BH}})$  for the Hernquist and the NFW model, as a function of  $M_{\text{halo}}/a_0$ , for different values of  $a_0$ . We fix  $r_c = 5a_0$  for the NFW profile. Results for the Hernquist case provide a fully numerical confirmation of the analysis presented in Ref. [24]. Changes with respect to the Schwarzschild solution can be interpreted in terms of a redshift scaling of the frequencies  $\Omega_{\text{LR}}/\Omega_{\text{LR}}^{\text{Scw}} \sim 1 - z$ , with  $z = M_{\text{halo}}/a_0$ . Such dependence becomes increasingly more accurate as  $z$  decreases, and for larger values of  $a_0$ , as shown in the inset of the panels, which provides a zoom on the low- $z$  regime.

Similar considerations hold for the ISCO frequencies. We have fitted our numerical data for  $a_0 \in [10^2, 10^7]M_{\text{BH}}$  and  $z \leq 0.001$  as

$$\frac{\Omega_{\text{LR,ISCO}}}{\Omega_{\text{LR,ISCO}}^{\text{Scw}}} = c_0 + c_1 z + c_2 z^2 + c_3 M_{\text{halo}}/a_0^2 , \quad (23)$$

recovering for the coefficients  $c_i$  the values found in closed form in Ref. [24], through a small  $z$  expansion of  $\Omega_{\text{LR,ISCO}}$ .

<sup>1</sup> We verified that larger values of  $n_{\text{in}}$  and  $n_{\text{out}}$  do not change our results to the precision required here.

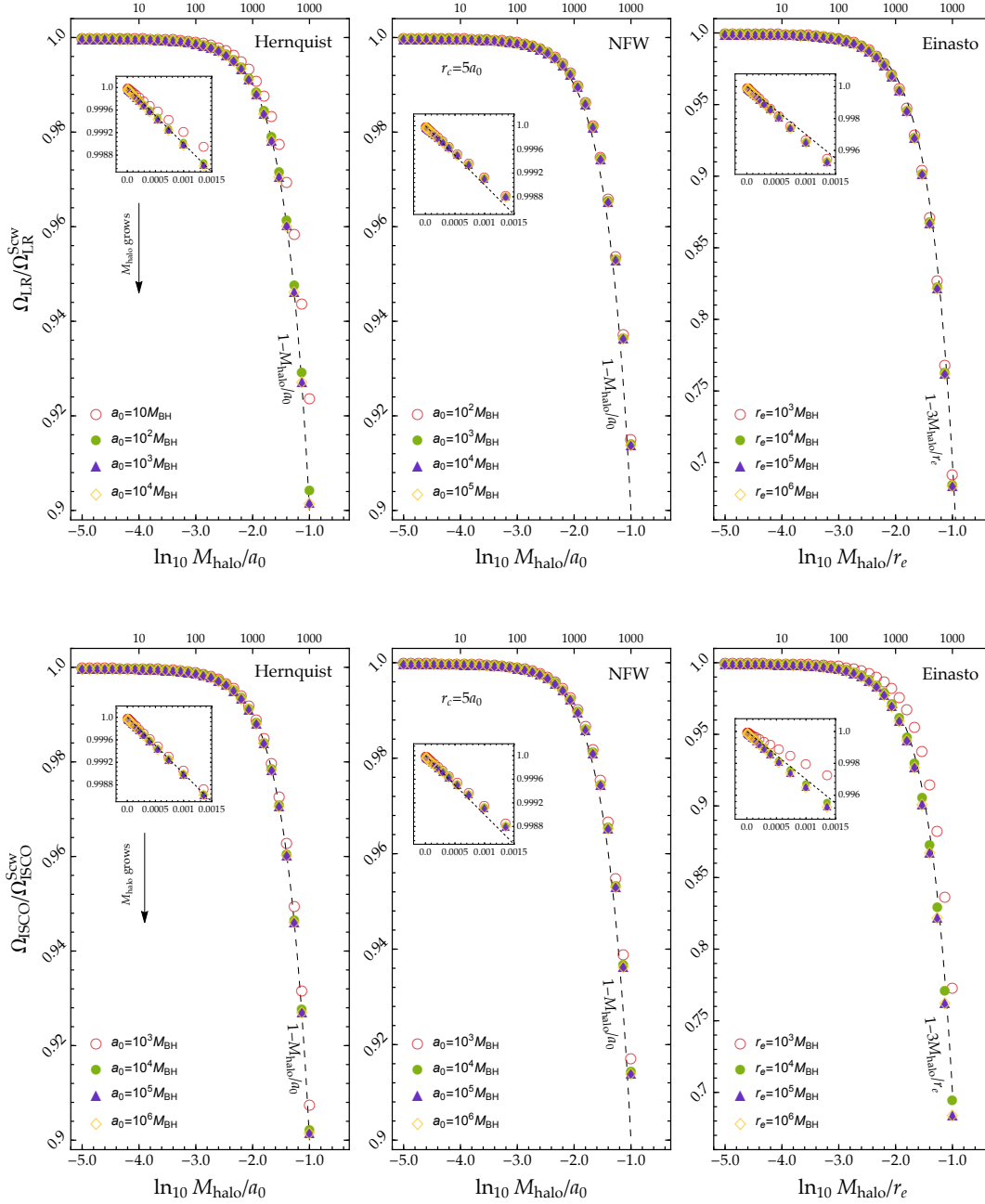


FIG. 3. **Top row:** Light ring frequencies as a function of the redshift parameter  $M_{\text{halo}}/a_0$  for the Hernquist and NFW profiles, and  $M_{\text{halo}}/r_e$  for the Einasto model. Frequencies are normalized to the Schwarzschild value  $\Omega_{\text{LR}}^{\text{Scw}} = 1/3\sqrt{3}M_{\text{BH}}$ . Different dots and colors refer to various choices of  $a_0$  and  $r_e$ . The arrow in the first panel on the left identifies the direction in which, for a given  $M_{\text{halo}}/a_0$  (and  $M_{\text{halo}}/r_e$ ),  $M_{\text{halo}}$  grows. The top axis show the values of the halo mass for a reference  $a_0 = 10^3 M_{\text{BH}}$  ( $r_e = 10^5 M_{\text{BH}}$ ). The black dashed line corresponds to a re-scaling of the frequencies  $\Omega_{\text{LR}} = \Omega_{\text{LR}}^{\text{Scw}}(1 - M_{\text{halo}}/a_0)$  for Hernquist and NFW, and  $\Omega_{\text{LR}} = \Omega_{\text{LR}}^{\text{Scw}}(1 - 3M_{\text{halo}}/r_e)$  for Einasto. For the NFW profile we show values of the frequencies for  $r_c = 5a_0$ . The inset in each panel shows a zoom on the low  $M_{\text{halo}}/a_0$  and  $M_{\text{halo}}/r_e$  regime. **Bottom row:** Same as top but for the orbital frequencies at the Innermost Stable Circular Orbits, with  $\Omega_{\text{ISCO}}^{\text{Scw}} = 1/6\sqrt{6}M_{\text{BH}}$ .



For  $z \lesssim 0.01$ , a simple scaling  $\Omega_{\text{LR,ISCO}} = \Omega_{\text{LR,ISCO}}^{\text{Scw}}(1-z)$  is able to reproduce the data with a relative errors smaller than 1%. This behavior also seems to apply to the NFW case, shown in the center panel of Fig. 3 assuming  $r_c = a_0$ . While the slope of the scaling depends on the actual value of  $r_c$ , for  $z$  smaller than  $10^{-3}$ , we recover an universal trend. Results for  $r_c = a_0$  and  $r_c = 2a_0$  are drawn in Fig. 4. Regardless of the specific choice of the cutoff, changes with respect to the vacuum case follow a  $M_{\text{halo}}/a_0$  scaling. We have explored different configurations within  $r_c \in [1, 5]a_0$  and  $a_0 \in [10^2, 10^7]M_{\text{BH}}$ . In this domain, for  $M_{\text{halo}}/a_0 \leq 0.01$  and  $M_{\text{halo}} > M_{\text{BH}}$  we find that the semi-analytic fits

$$\frac{\Omega_{\text{LR}}}{\Omega_{\text{LR}}^{\text{Scw}}} = 1 - \frac{p_1 z}{(r_c/a_0)p_2}, \quad \frac{\Omega_{\text{ISCO}}}{\Omega_{\text{ISCO}}^{\text{Scw}}} = 1 - \frac{s_1 z}{(r_c/a_0)s_2}, \quad (24)$$

where  $(p_1, p_2, s_1, s_2) = (2.546, 0.698, 2.535, 0.6956)$ , are able to describe our numerical results with relative accuracy better than  $\sim 0.1\%$ .

Finally, the right panels of Fig. 3 show the geodesics analysis for the Einasto model. In this case deviations from Schwarzschild for both the light ring and ISCO frequencies highlight a dependence on  $M_{\text{halo}}/r_e$ . As  $r_e$  increases  $\Omega_{\text{LR,ISCO}}/\Omega_{\text{LR,ISCO}}^{\text{Scw}}$  follow a scaling  $\sim 1 - 3M_{\text{halo}}/r_e$ , which becomes independent from  $r_e$  as  $M_{\text{halo}}/r_e$  decreases.

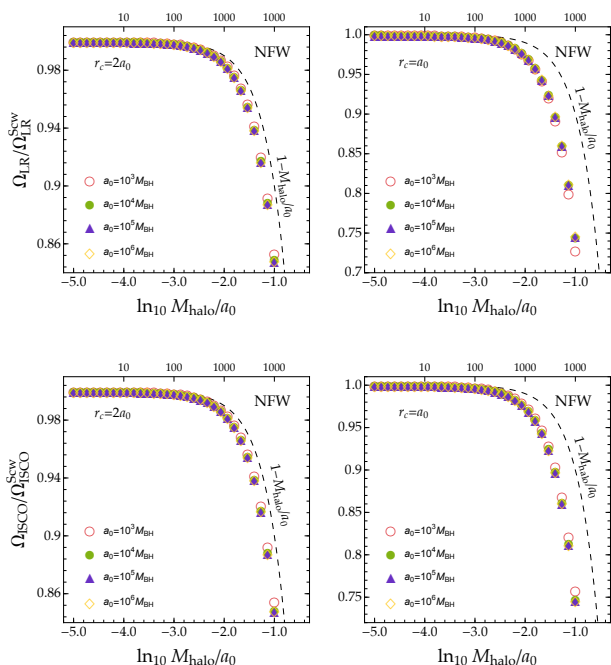


FIG. 4. Light ring (top) and ISCO (bottom) frequencies for the NFW density profile as a function of  $M_{\text{halo}}/a_0$ , normalised to the corresponding Schwarzschild values, for different  $a_0$ . Left and right panels correspond to a cut-off radius for the matter distribution of  $r_c = 2a_0$  and  $r_c = a_0$ . The Top axis identify the halo mass  $M_{\text{halo}}/M_{\text{BH}}$  for  $a_0 = 10^5 M_{\text{BH}}$ .

$\ell$	$ m $	Schw	Hernquist	NFW	NFW	Einasto
				$r_c = a_0$	$r_c = 5a_0$	$r_e = a_0$
2	1	7.8175e-7	7.8019e-7	7.7771e-7	7.8039e-7	7.7642e-7
3	2	2.3974e-7	2.3926e-7	2.3850e-7	2.3933e-7	2.3811e-7
4	1	7.9715e-13	7.9555e-13	7.9301e-13	7.9576e-13	7.9158e-13
4	3	5.4572e-8	5.4462e-8	5.4290e-8	5.4477e-8	5.4200e-8

TABLE I. Axial fluxes (normalized to  $m_p^2/M_{\text{BH}}^2$ ) for a secondary sitting at  $r_p = 8M_{\text{BH}}$ . We focus on halo configurations with  $M_{\text{halo}}/a_0 = 10^{-3}$  and  $a_0 = 10^5 M_{\text{BH}}$ . For the Einasto profile we assume  $r_e = a_0$ .

## B. Gravitational-wave emission

We can now focus on the axial GW emission. Tables I-II show the values of the energy released at infinity for different mode configurations, compared against the vacuum components. We computed the latter through the Black Hole Perturbation Toolkit [39]. For a given BH mass, GW fluxes are smaller in the case of non-vacuum environments, and decrease as the compactness of the halo, either,  $M_{\text{halo}}/a_0$  or  $M_{\text{halo}}/r_e$ , grows. For the NFW model this behavior also depends on the cutoff radius, with  $\dot{E}_{\ell m}^\infty$  becoming smaller as  $r_c$  shrinks. As shown in [24] however, differences between the Schwarzschild and the halo case can be interpreted, for the axial sector, in terms of a redshift effect. Our results support this picture across different halo models. Figure 5 shows indeed the relative difference between matter and vacuum fluxes as a function of the GW frequency, for the  $(\ell, m) = (2, 1)$  mode, and  $M_{\text{halo}} = 10^2 M_{\text{BH}}$ . Dashed (solid) curves correspond to redshifted (unredshifted) fluxes in vacuum, obtained by scaling

$$\Omega^{\text{vac}} \rightarrow \Omega/\gamma, \quad m_p^{\text{vac}} \rightarrow m_p \gamma, \quad \omega^{\text{vac}} \rightarrow \omega/\gamma, \quad (25)$$

where  $\gamma = 1 - \delta M_{\text{halo}}/a_0$  for the Hernquist and NFW profiles and  $\gamma = 1 - \delta M_{\text{halo}}/r_e$  for the Einasto model. In agreement with the geodesic analysis, we find the best match between the Schwarzschild and halo fluxes assuming  $\delta = 1$ ,  $\delta \sim 0.9$  in the first two cases, and  $\delta \sim 3$  for the Einasto distribution. The latter yields in general the largest differences with respect to the vacuum evolution. The agreement between the redshift and matter results improves again for less dense halos, and deteriorates only for very compact (and unrealistic) configurations with  $M_{\text{halo}}/a_0 = 0.1$ .

## V. CONCLUSIONS

Our work provides a step forward towards a general relativistic description of compact sources evolving within non-trivial environments. We have extended the analysis carried out in Ref. [6, 24], developing a numerical approach to find BH solutions embedded in an anisotropic fluid with

$\ell$	$ m $	Schw	Hernquist	NFW	NFW	Einasto
				$r_c = a_0$	$r_c = 5a_0$	$r_e = a_0$
2	1	7.8175e-7	6.3598e-7	4.3470e-7	6.5338e-7	4.1168e-7
3	2	2.3974e-7	1.9545e-7	1.3408e-7	2.0060e-7	1.3085e-7
4	1	7.9715e-13	6.0233e-13	3.6128e-13	6.4033e-13	1.6413e-13
4	3	5.4572e-8	4.4570e-8	3.0668e-8	4.5706e-8	3.0968e-8

TABLE II. Same as Table I but for an halo with  $M_{\text{halo}}/a_0 = 10^{-1}$ .

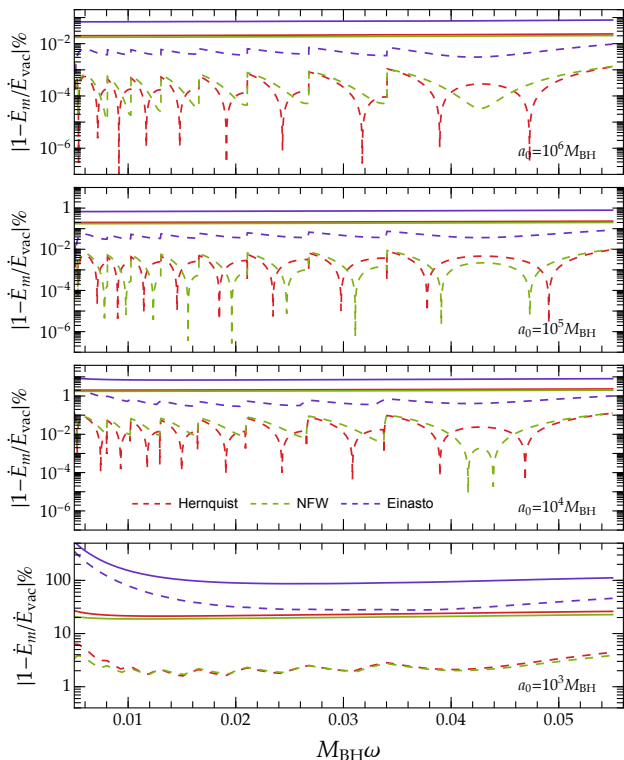


FIG. 5. Relative percentage difference between the matter and vacuum axial  $\ell = 2$   $m = 1$  flux emitted by an EMRI, as a function of the GW frequency. We assume  $M_{\text{halo}} = 100M_{\text{BH}}$  for the halo configuration. Fluxes for the NFW and the Einasto model are obtained fixing  $r_c = 5a_0$  and  $r_e = a_0$ , respectively. Dashed (solid) lines correspond to relative differences with respect vacuum redshifted (unredshifted) results.

a generic density profile. We have exploited this approach to study the impact of different DM distributions on the BH spacetime, and on the evolution of very asymmetric binaries, with small mass ratios.

While changes with respect to vacuum backgrounds depend on the specific setup, our results confirm the existence of features common to different models. Deviations from Schwarzschild predictions scale with the halo density and increase in the presence of overdensities close to

the BH horizon, as spikes induced by matter accretion. Such changes however can be interpreted, and quantified, in terms of redshift of the geodesic properties and of the GW frequencies. For halo models belonging to the two-parameter family described by Eq. (15), like the Hernquist and the NFW profiles, the redshift scaling approaches a universal behavior when the halo compactness  $M_{\text{halo}}/a_0$  becomes smaller than  $10^{-3}$ . Similar considerations hold for the Einasto distribution, for which redshift of frequencies and fluxes is dictated by the spatial scale of the profile.

While the approach we have developed is completely general, our numerical results assume a simple prescription to describe the DM accretion onto the BH. We have explored the dependence of our conclusions on such assumption by adopting a second scaling of the halo profile,  $\rho(r) \rightarrow \rho(r)(1 - 4M_{\text{BH}}/r)$ , which mimics the correct behavior found by fully relativistic calculations of adiabatic accretion [23]. We have studied the properties of the geodesic motion and of the axial emission, finding for both a qualitative agreement with the analysis discussed in Sec. IV.

The details of the matter distribution, however, can be relevant to accurately determine the actual evolution of binaries throughout the coalescence, and build waveform models for next generation of detectors [14]. We are working to include the full general relativity treatment of the the DM spike distribution within the formalism devised in this work, further extending the set of gravitational perturbations to the polar sector. The results of such analysis will be presented in a forthcoming paper with a full adiabatic evolution of EMRI in non-vacuum environments.

**Acknowledgments.** E.F. acknowledges financial support from ENS de Lyon. This work makes use of the Black Hole Perturbation Toolkit. V.C. is a Villum Investigator and a DNRF Chair, supported by VILLUM Foundation (grant no. VIL37766) and the DNRF Chair program (grant no. DNRF162) by the Danish National Research Foundation. V.C. acknowledges financial support provided under the European Union’s H2020 ERC Advanced Grant “Black holes: gravitational engines of discovery” grant agreement no. Gravitas–101052587. Views and opinions expressed are however those of the author only and do not necessarily reflect those of the European Union or the European Research Council. Neither the European Union nor the granting authority can be held responsible for them. This project has received funding from the European Union’s Horizon 2020 research and innovation programme under the Marie Skłodowska-Curie grant agreement No 101007855. We thank FCT for financial support through Projects No. UIDB/00099/2020 and UIDB/04459/2020. We acknowledge financial support provided by FCT/Portugal through grants 2022.01324.PTDC, PTDC/FIS-AST/7002/2020, UIDB/00099/2020 and UIDB/04459/2020.

- 
- [1] N. Yunes, B. Kocsis, A. Loeb, and Z. Haiman, *Phys. Rev. Lett.* **107**, 171103 (2011), arXiv:1103.4609 [astro-ph.CO].
- [2] E. Barausse, V. Cardoso, and P. Pani, *Phys. Rev. D* **89**, 104059 (2014), arXiv:1404.7149 [gr-qc].
- [3] V. Cardoso and A. Maselli, *Astron. Astrophys.* **644**, A147 (2020), arXiv:1909.05870 [astro-ph.HE].
- [4] V. Cardoso, C. F. B. Macedo, and R. Vicente, *Phys. Rev. D* **103**, 023015 (2021), arXiv:2010.15151 [gr-qc].
- [5] A. Derdzinski, D. D’Orazio, P. Duffell, Z. Haiman, and A. MacFadyen, *Mon. Not. Roy. Astron. Soc.* **501**, 3540 (2021), arXiv:2005.11333 [astro-ph.HE].
- [6] V. Cardoso, K. Destounis, F. Duque, R. Panosso Macedo, and A. Maselli, *Phys. Rev. Lett.* **129**, 241103 (2022), arXiv:2210.01133 [gr-qc].
- [7] L. Zwick, P. R. Capelo, and L. Mayer, (2022), arXiv:2209.04060 [gr-qc].
- [8] V. Cardoso, T. Ikeda, R. Vicente, and M. Zilhão, *Phys. Rev. D* **106**, L121302 (2022), arXiv:2207.09469 [gr-qc].
- [9] Z. Pan, Z. Lyu, and H. Yang, *Phys. Rev. D* **104**, 063007 (2021), arXiv:2104.01208 [astro-ph.HE].
- [10] V. De Luca, A. Maselli, and P. Pani, *Phys. Rev. D* **107**, 044058 (2023), arXiv:2212.03343 [gr-qc].
- [11] L. Sberna *et al.*, *Phys. Rev. D* **106**, 064056 (2022), arXiv:2205.08550 [gr-qc].
- [12] L. Speri, A. Antonelli, L. Sberna, S. Babak, E. Barausse, J. R. Gair, and M. L. Katz, (2022), arXiv:2207.10086 [gr-qc].
- [13] B. J. Kavanagh, D. A. Nichols, G. Bertone, and D. Gaggero, *Phys. Rev. D* **102**, 083006 (2020), arXiv:2002.12811 [gr-qc].
- [14] N. Speeney, A. Antonelli, V. Baibhav, and E. Berti, *Phys. Rev. D* **106**, 044027 (2022), arXiv:2204.12508 [gr-qc].
- [15] C. F. B. Macedo, P. Pani, V. Cardoso, and L. C. B. Crispino, *Astrophys. J.* **774**, 48 (2013), arXiv:1302.2646 [gr-qc].
- [16] K. Eda, Y. Itoh, S. Kuroyanagi, and J. Silk, *Phys. Rev. Lett.* **110**, 221101 (2013), arXiv:1301.5971 [gr-qc].
- [17] A. Maselli, N. Franchini, L. Gualtieri, T. P. Sotiriou, S. Barsanti, and P. Pani, *Nature Astron.* **6**, 464 (2022), arXiv:2106.11325 [gr-qc].
- [18] R. Brito, V. Cardoso, and P. Pani, *Lect. Notes Phys.* **906**, pp.1 (2015), arXiv:1501.06570 [gr-qc].
- [19] S. Babak, H. Fang, J. R. Gair, K. Glampedakis, and S. A. Hughes, *Phys. Rev. D* **75**, 024005 (2007), [Erratum: *Phys.Rev.D* **77**, 04990 (2008)], arXiv:gr-qc/0607007.
- [20] K. Destounis, A. G. Suvorov, and K. D. Kokkotas, *Phys. Rev. Lett.* **126**, 141102 (2021), arXiv:2103.05643 [gr-qc].
- [21] R. Vicente and V. Cardoso, *Phys. Rev. D* **105**, 083008 (2022), arXiv:2201.08854 [gr-qc].
- [22] D. Traykova, K. Clough, T. Helfer, E. Berti, P. G. Ferreira, and L. Hui, *Phys. Rev. D* **104**, 103014 (2021), arXiv:2106.08280 [gr-qc].
- [23] L. Sadeghian, F. Ferrer, and C. M. Will, *Phys. Rev. D* **88**, 063522 (2013), arXiv:1305.2619 [astro-ph.GA].
- [24] V. Cardoso, K. Destounis, F. Duque, R. P. Macedo, and A. Maselli, *Phys. Rev. D* **105**, L061501 (2022), arXiv:2109.00005 [gr-qc].
- [25] L. Hernquist, *Astrophys. J.* **356**, 359 (1990).
- [26] A. Einstein, *Annals Math.* **40**, 922 (1939).
- [27] T. Regge and J. A. Wheeler, *Phys. Rev.* **108**, 1063 (1957).
- [28] F. J. Zerilli, *Phys. Rev. D* **2**, 2141 (1970).
- [29] L. Lindblom and S. L. Detweiler, *Astrophys. J. Suppl.* **53**, 73 (1983).
- [30] K. S. Thorne and A. Campolattaro, *Non-Radial Pulsation of General-Relativistic Stellar Models. I. Analytic Analysis for  $L \geq 2$* , *Astrophysical Journal*, vol. 149, p.591 (1967).
- [31] A. W. Graham, D. Merritt, B. Moore, J. Diemand, and B. Terzic, *Astron. J.* **132**, 2685 (2006), arXiv:astro-ph/0509417.
- [32] J. F. Navarro, C. S. Frenk, and S. D. M. White, *Astrophys. J.* **490**, 493 (1997), arXiv:astro-ph/9611107.
- [33] J. Einasto, *Astrofizika* **5**, 137 (1969).
- [34] F. Prada, A. A. Klypin, E. Simonneau, J. Betancort-Rijo, S. Patiri, S. Gottlober, and M. A. Sanchez-Conde, *Astrophys. J.* **645**, 1001 (2006), arXiv:astro-ph/0506432.
- [35] P. Gondolo and J. Silk, *Phys. Rev. Lett.* **83**, 1719 (1999), arXiv:astro-ph/9906391.
- [36] sgrep repo, ([github.com/masellia/SGREP/](https://github.com/masellia/SGREP/)).
- [37] K. Akiyama *et al.* (Event Horizon Telescope), *Astrophys. J. Lett.* **875**, L1 (2019), arXiv:1906.11238 [astro-ph.GA].
- [38] GRAVITY Collaboration, R. Abuter, A. Amorim, M. Bauböck, J. P. Berger, H. Bonnet, W. Brandner, Y. Clénet, V. Coudé Du Foresto, P. T. de Zeeuw, C. Deen, J. Dexter, G. Duvert, A. Eckart, F. Eisenhauer, N. M. Förster Schreiber, P. Garcia, F. Gao, E. Gendron, R. Genzel, S. Gillessen, P. Guajardo, M. Habibi, X. Haubois, T. Henning, S. Hippler, M. Horrobin, A. Huber, A. Jiménez-Rosales, L. Jocou, P. Kervella, S. Lacour, V. Lapeyrière, B. Lazareff, J. B. Le Bouquin, P. Léna, M. Lippa, T. Ott, J. Panduro, T. Paumard, K. Perraut, G. Perrin, O. Pfuhl, P. M. Plewa, S. Rabien, G. Rodríguez-Coira, G. Rousset, A. Sternberg, O. Straub, C. Straubmeier, E. Sturm, L. J. Tacconi, F. Vincent, S. von Fellenberg, I. Waisberg, F. Widmann, E. Wieprecht, E. Wieszorek, J. Woillez, and S. Yazici, *Astronomy & Astrophysics* **618**, L10 (2018), arXiv:1810.12641 [astro-ph.GA].
- [39] Black Hole Perturbation Toolkit, ([bhptoolkit.org](https://bhptoolkit.org/)).